Intrinsically Organised Resting State Networks in the Human Spinal Cord

Kong, Eippert, Beckmann, Andersson, Finsterbusch, Büchel, Tracey and Brooks

Supplementary Information Appendix

Materials and Methods

Data acquisition: Resting state fMRI data was collected as the last session in a larger spinal fMRI experiment consisting of two sensory and two motor sessions. During all sessions a white crosshair was shown on the screen, which turned red every 15s; subjects were asked to stay as still as possible with eyes open. Subjects were imaged with a 12-channel head coil combined with a 4-channel neck coil (both receive-only), with the cervical spinal cord centered in the neck coil and positioned at isocenter in the magnet. Resting state GE-EPI fMRI data were acquired with following parameters: number of volumes = 250, TR = 1890ms, TE = 44ms, flip-angle = 80°, in-plane resolution of 1.0mm (matrix 128x128), slice thickness = 5.0mm, 16 transversal slices covering vertebrae C4-T1, phase encoding A>>P and GRAPPA factor 2. To minimise sensitivity to flow effects, flow rephasing in the slice direction and spatially selective saturation pulses superior and inferior to the target volume were used and coil channel data were combined with a sum-of-squares algorithm. Furthermore, additional saturation pulses were applied posterior and anterior to the target region, i.e. in the phase-encoding direction, in order to minimise pulsatile blood flow artefacts. The adjustments prior to the functional acquisitions (i.e. shimming) were performed on a manually defined volume of about 35x30x70mm^3 covering the target region in the spinal cord. Only the

neck-coil was used for acquisition of fMRI data. High-resolution (1.0×1.0×1.0 mm voxel size) T1-weighted images were also acquired for each subject using a MPRAGE sequence (sagittal slice orientation, repetition time 2.3s, echo time 3.5ms, readout flip angle 9°, inversion time 1.1s, field-of-view 192x240x256mm^3). The field of view for this acquisition ranged from the top of the midbrain to the second thoracic vertebra and both the neck coil and the head coil were used for data acquisition.

Data pre-processing: In the physiological noise model, cardiac, respiratory and interaction effects were modeled using Fourier series as described previously (1, 2), resulting in a total of 32 regressors. Additional nuisance regressors consisted of a) low frequency cerebrospinal fluid (CSF) signal (extracted from voxels whose variance lay in the top 10 percentile within a region including both the spinal cord and CSF space), b) heart rate (value of the smoothed beats per minute (BPM) trace at the acquisition time for each slice), c) motion correction parameters (x and y translation), and d) a regressor that modelled the color-change of the cross-hair that was presented on the screen.

Registration of functional images to the structural volume was initialised using the scanner *sqform* transformation. Due to EPI distortion in the fMRI data, there remained residual mismatch between the structural and functional data in some slices following the initial transformation. We therefore applied an additional slice-wise registration procedure (x and y translations) on these data (based on hand-drawn spinal cord masks), which minimised the mismatch, and brought fMRI data into good alignment with each subject's structural volume.

To allow for data analysis in a common anatomical space, we first identified a subject with minimal anterior-posterior and left-right curvature of the spine: this subject became the experimental "standard template". Subsequently, each participant's

structural image was registered to this template using FMRIB's non-linear image registration tool (FNIRT; details: 40 iterations, changing warp resolution from 10mm to 1mm, bias field modeling resolution of 20mm and weighting lambda of 100, weighting mask covering spinal cord and disks/vertebrae) and finally the sqform, XY translation and non-linear warping were applied to the functional data to bring it into a common anatomical space (resampled at 1x1x1mm). We also applied these parameters to hand-drawn spinal cord masks, which were then averaged to generate a group cord mask, in which group data analysis was performed. Note that this mask only included voxels that were present in every participant's individual mask (i.e. the intersection of all masks). We also created a dilated version of this group cord mask, in order to allow the investigation of signal components present in the CSF space surrounding the cord.

Control for white matter effects: In order to demonstrate that signals arising from the spinal cord white matter do not contaminate the observed results, we repeated the original analyses after white matter signals had been regressed out. To this end, we first registered the MNI-Poly-AMU template (3) to our own template, using the registration functions contained in the Spinal Cord Toolbox (sourceforge.net/projects/spinalcordtoolbox; (4)), and then brought it into individual subject-space using FNIRT. Thereafter, we thresholded the probabilistic white-matter map of the MNI-Poly-AMU template at 0.9 and used this as a mask to extract the first principal component of white matter signal for every slice in every subject. These components were then added to our physiological noise model so that they could be regressed out of the functional data, and finally ICA was performed on the residuals of the functional data as described previously. To test for the similarity between the results

of the original analysis and this control analysis, we used spatial correlation against the original components.

Control for CSF effects: As our original group ICA was restricted to the spinal cord (which was defined by a spinal cord group mask), we wanted to rule out the possibility that the identified components might be drawn from signal fluctuations in the surrounding CSF (despite the fact that we had regressed out CSF-effects on a slice-wise basis as part of our physiological clean-up procedure). A separate group ICA (using 90 components) was therefore performed using a mask that incorporated the spinal cord and the subarachnoid space that contains CSF. RSNs of interest within this extended mask were then obtained by using spatial correlation against the previously defined RSNs within the cord mask.

Reliability and reproducibility: In order to investigate the reliability of the observed spinal RSNs, we split our data set in half (i.e. each subject's 250 volume time-series was split into two 125 volume time-series) and then employed the procedures described in Zuo et al. (5) (see their Figure 1). In brief, for each of the 24 components that we identified as ventral or dorsal RSNs (Figure 1 & 2), we first used dual regression on each of the halved individual data sets in order to reconstruct this component at the split individual level. Next, we estimated the voxel-wise split-half reliability for each of these components by calculating intra-class correlation coefficient (ICC) maps, using the ICC formulation employed by Zuo et al. (5) (see their Appendix for its computation) and thresholded the resulting maps at an ICC level of 0.4 (ICCs generally range from -1 to 1, with the ICCs < 0.40 denoting poor reliability, ICCs between 0.40 and 0.59 denoting fair reliability, ICCs between 0.60 and 0.74 denoting good reliability and ICCs between 0.75

and 1.00 denoting excellent reliability (6)). We also report the percentage of voxels within each component map that survive a thresholding at values of 0.4 (fair reliability) and 0.6 (good reliability).

To estimate the reproducibility of the group ICA components at the individual level, we first ran a single-session ICA on each of the individual data sets (i.e. 20 ICAs in total) and then carried out a template matching against the group ICA results: for each of the dorsal and ventral components displayed in Figure 1 & 2, we determined the maximum spatial correlation between the components of an individual ICA and this template component and noted down the component from which this maximum correlation arose. This was iterated over all 24 group components and all 20 individual ICAs, and allowed us to estimate how reproducible individually determined spinal RSNs are (Figure S11, blue lines). We then supplemented this analysis by matching individual ICA components against a different template, namely one that was created on an individual basis by using dual regression (Figure S11, red lines). Finally, for the sake of completeness we investigated the degree of discordance between these two template-matching options, i.e. the number of cases (out of 20), where a different component showed the maximum spatial correlation with the group ICA template and the dual regression template (Figure S11, numbers at the bottom). This last part is not of primary importance but was done in order to have this analysis as similar to that of Zuo et al. (2010) (5) as possible and give a descriptive indication of the robustness in comparison to the data obtained from the brain.

References

1. Brooks JC*, et al.* (2008) Physiological noise modelling for spinal functional magnetic resonance imaging studies. *NeuroImage* 39(2):680-692.
2. Kong Y, Jenkinson M, Andersson J, Tracey I, & Brooks JC (2012) Assessment of physiological noise modelling methods for functional imaging of the spinal cord. *NeuroImage* 60(2):1538-1549.
3. Fonov VS*, et al.* (2014) Framework for integrated MRI average of the spinal cord white and gray matter: The MNI-Poly-AMU template. *Neuroimage* 102P2:817-827.
4. Cohen-Adad J DLB, Benhamou M, Cadotte D, Fleet D, Cadotte A, Fehlings MG, Pelletier Paquette JP, Thong W, Taso M, Collins DL, Callot V, Fonov V. (2014) Spinal Cord Toolbox: an open-source framework for processing spinal cord MRI data. *Proceedings of the 20th Annual Meeting of OHBM, Hamburg, Germany* 3633.
5. Zuo XN*, et al.* (2010) Reliable intrinsic connectivity networks: test-retest evaluation using ICA and dual regression approach. *NeuroImage* 49(3):2163-2177.
6. Hallgren KA (2012) Computing Inter-Rater Reliability for Observational Data: An Overview and Tutorial. *Tutorials in quantitative methods for psychology* 8(1):23-34.

SI Appendix Figures

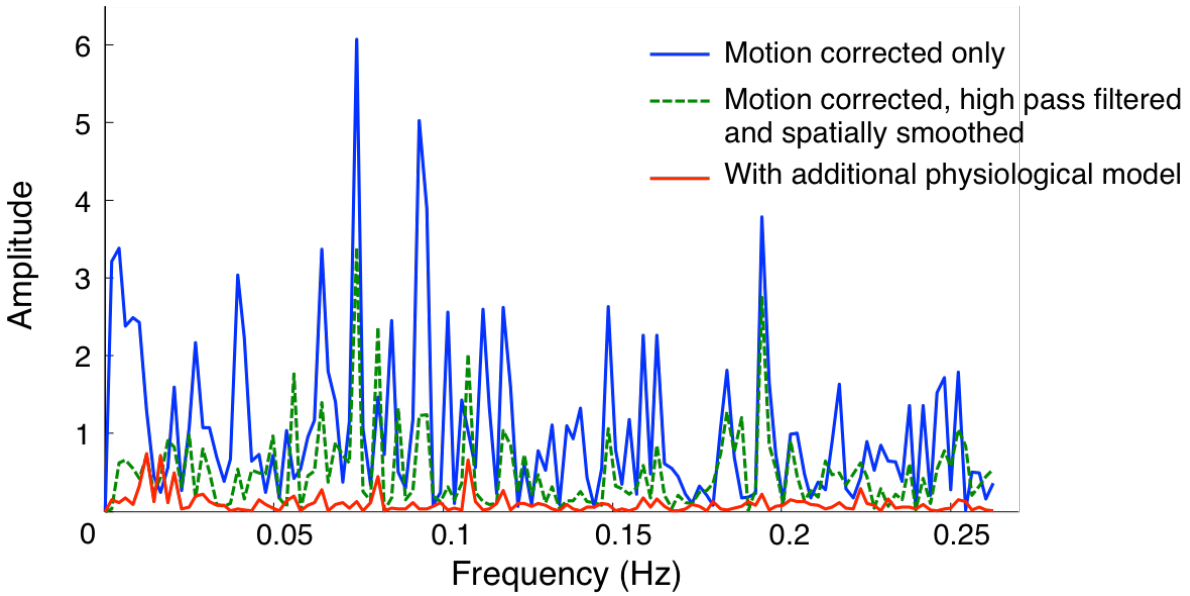

Figure S1. Group-average spinal cord power spectra. Depicted are power spectra of the data after different stages of pre-processing: (i) motion correction (MC) only, (ii) MC plus high-pass filtering (HPF) and spatial smoothing (SS), and (iii) MC+HPF+SS plus physiological noise modelling. High-pass filtering and spatial smoothing only removed very low frequency drift, whereas high frequency noise was effectively suppressed by using a validated physiological noise model.

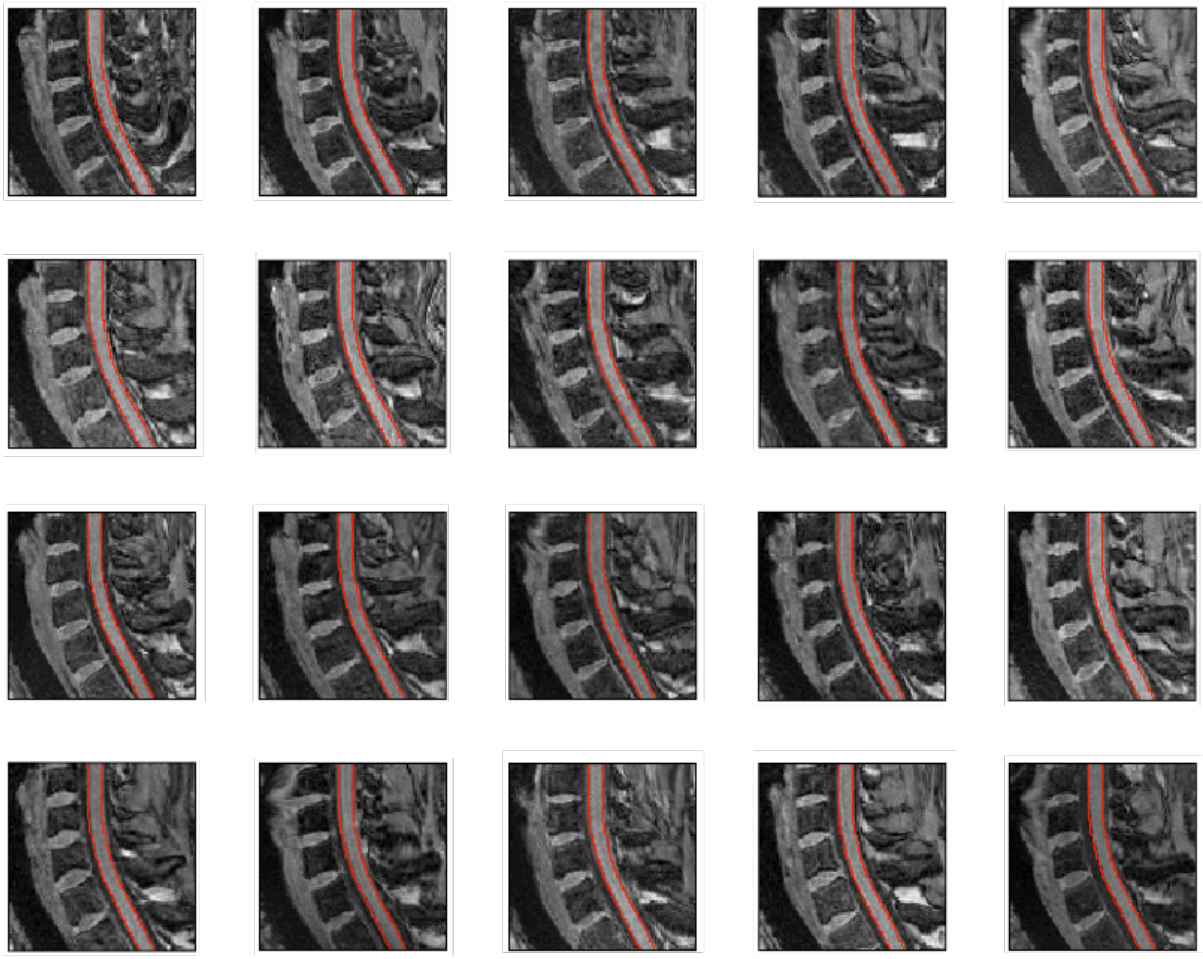

Figure S2. Accuracy of spatial normalisation. Depicted are mid-sagittal slices of each subject's spatially normalised anatomical image (vertebral levels C4-T1), upon which we overlaid a contour that represents the spinal cord outline of our template image. There is excellent overlap between the template and each individual image across the whole rostro-caudal extent.

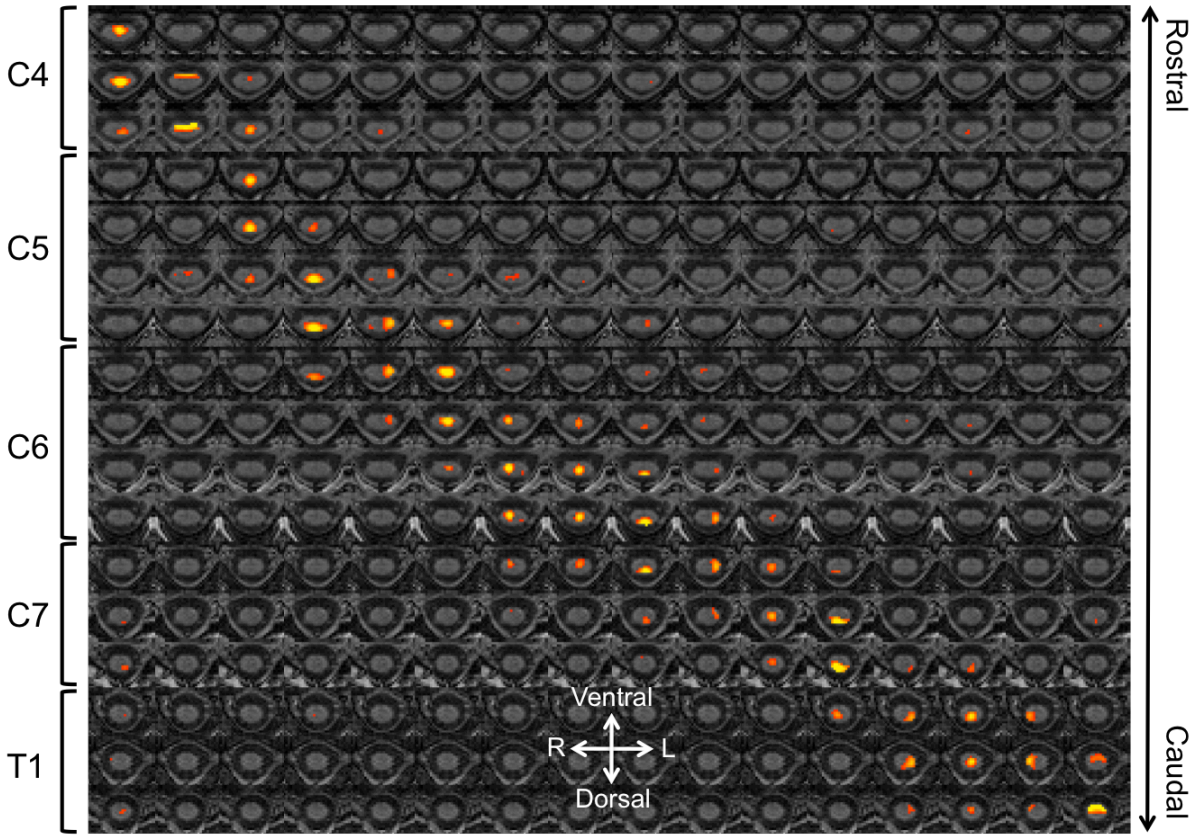

Figure S3. Spinal cord RSNs that were not selected as dorsal or ventral networks. Some of these likely reflect central canal CSF fluctuations, whereas a few others span both dorsal and ventral parts of the spine. Each RSN map is thresholded at FDR $p < 0.05$ and shown in rostro-caudal direction, overlaid on transversal sections of the template T1-weighted image.

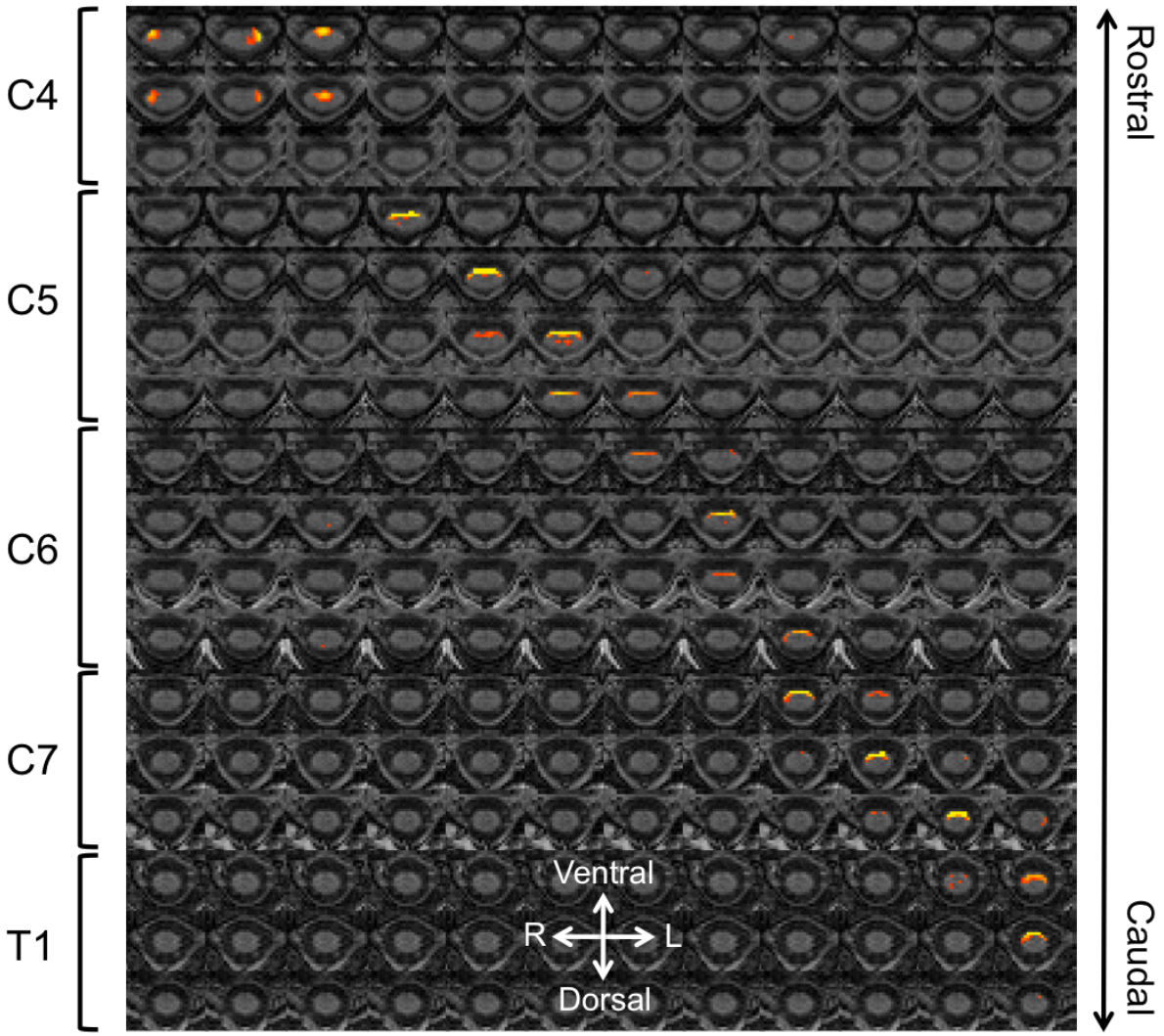

Figure S4. Ventral spinal RSNs from unsmoothed data. These components were identified by spatial correlation against the previously identified ventral RSNs. Importantly, despite the lack of spatial smoothing the components are still mostly bilateral. Each RSN map is thresholded at FDR $p < 0.05$ and shown in rostro-caudal direction, overlaid on transversal sections of the template T1-weighted image.

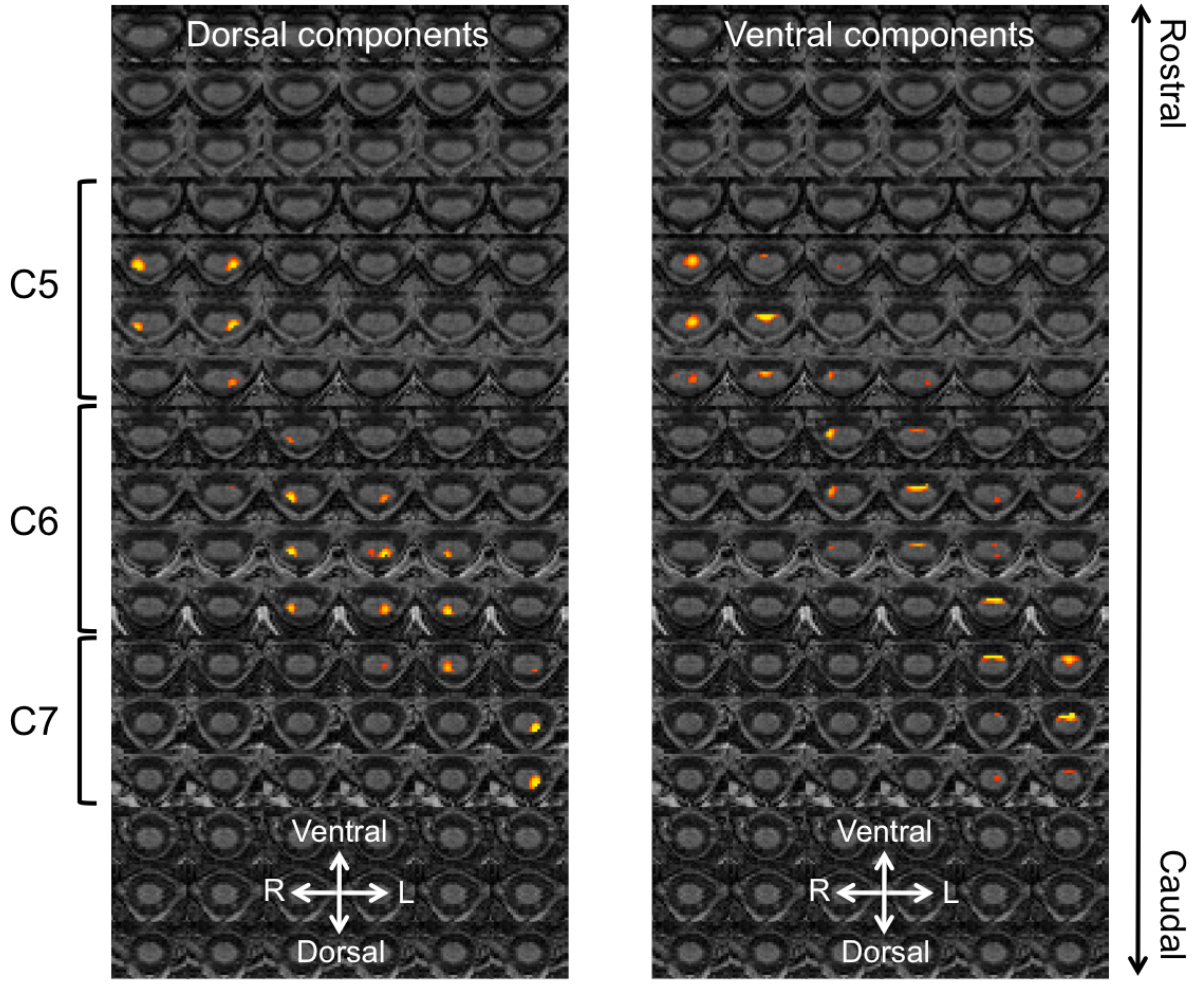

Figure S5. Dorsal and ventral spinal RSNs obtained from a reduced data-set spanning vertebral levels C5-C7. These components were identified by spatial correlation against the previously identified dorsal and ventral RSNs. Importantly, the rostro-caudal extent of the components is similar to that observed in the full data-set (Figures 1 & 2). Each RSN map is thresholded at FDR $p < 0.05$ and shown in rostro-caudal direction, overlaid on transversal sections of the template T1-weighted image.

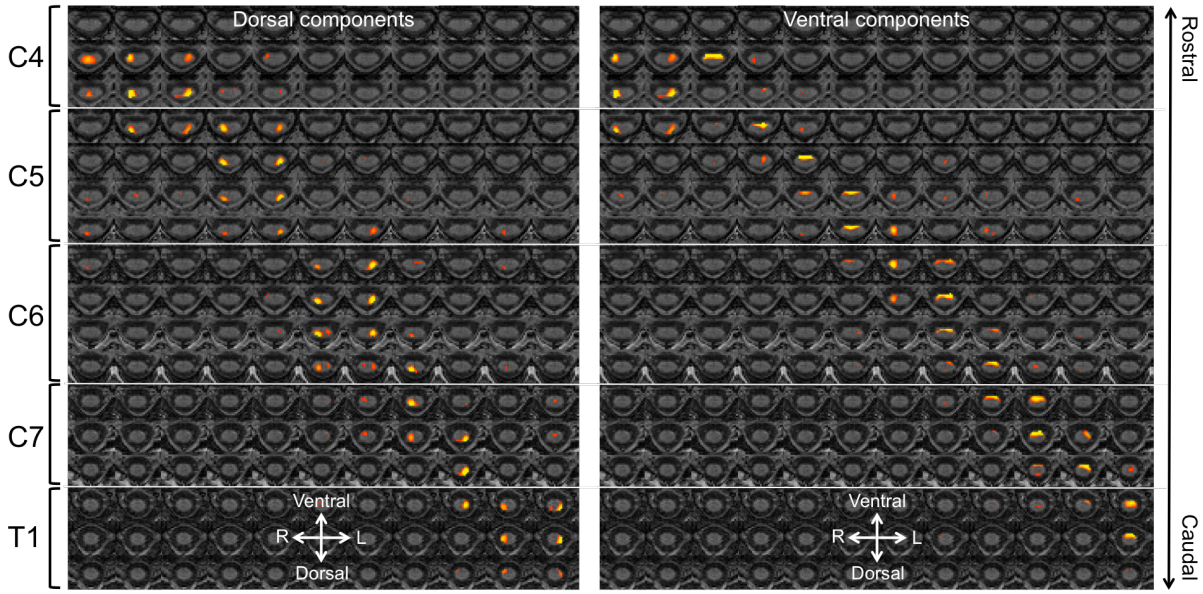

Figure S6. Dorsal and ventral spinal RSNs after white-matter signals had been regressed out. These components were identified by spatial correlation against the previously identified dorsal and ventral RSNs. The general pattern from the original data (Figures 1 & 2) is clearly preserved. Each RSN map is thresholded at FDR $p < 0.05$ and shown in rostro-caudal direction, overlaid on transversal sections of the template T1-weighted image.

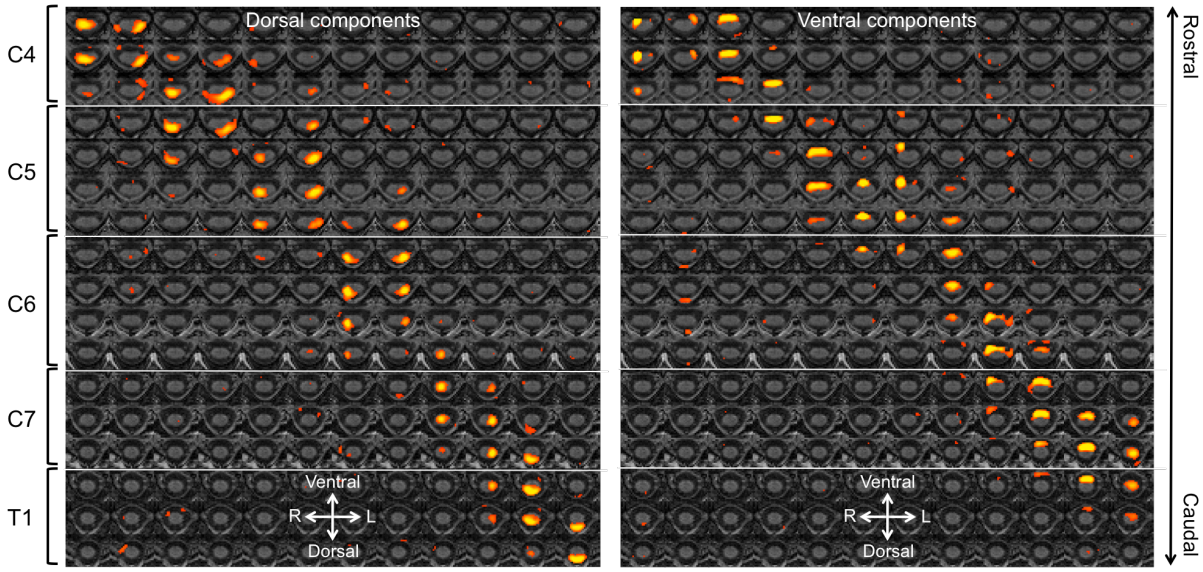

Figure S7. Dorsal and ventral spinal RSNs including CSF space. These components were identified by spatial correlation against the previously identified RSNs within the spinal cord. Each RSN map is thresholded at FDR $p < 0.05$ and shown in rostro-caudal direction, overlaid on transversal sections of the template T1-weighted image.

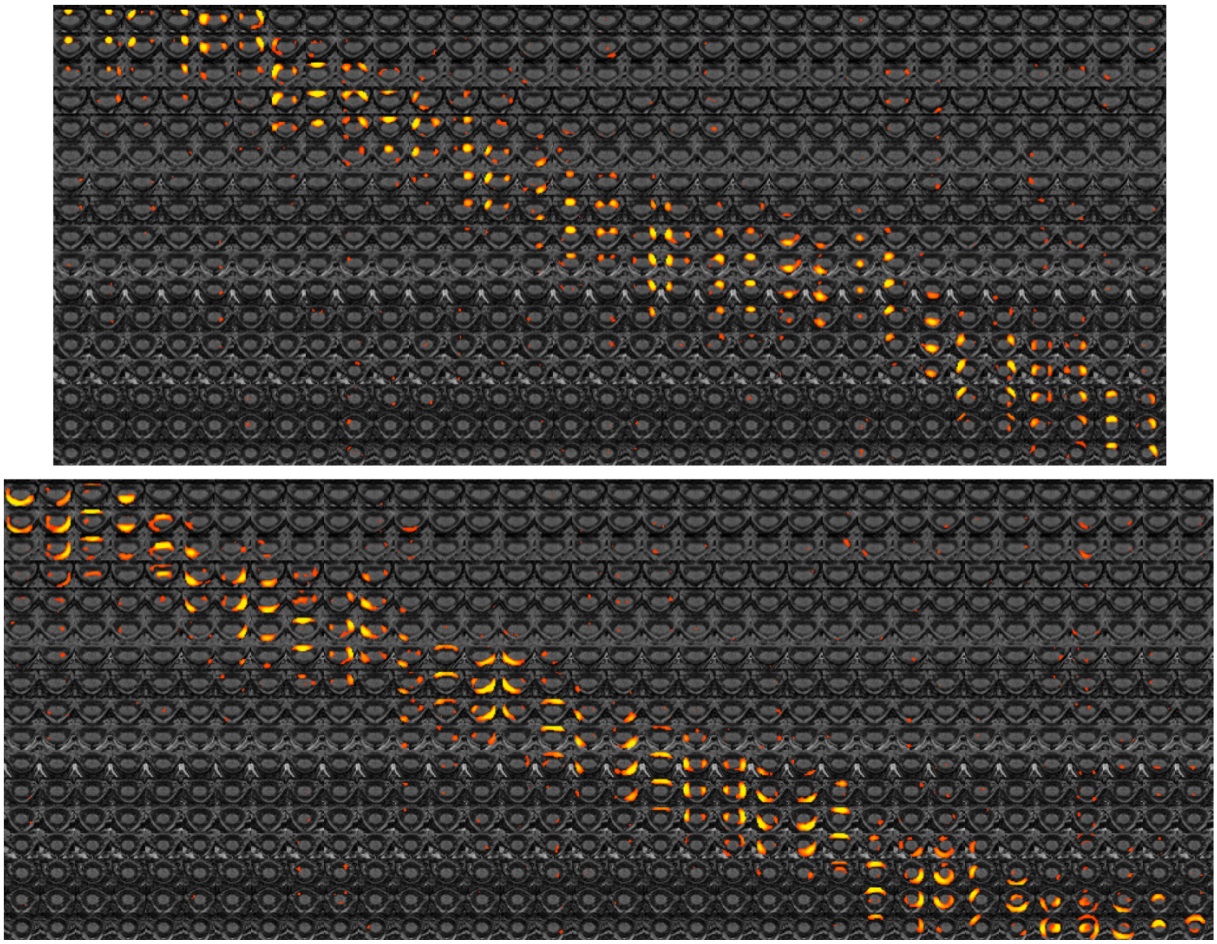

Figure S8. RSNs including CSF space that were not selected as dorsal or ventral networks. These components have a strikingly different spatial profile than the selected ones and most likely correspond to effects induced by blood vessels (upper panel), remaining CSF fluctuations or remaining motion artefacts (lower panel). Each RSN map is thresholded at FDR $p < 0.05$ and shown in rostro-caudal direction, overlaid on transversal sections of the template T1-weighted image.

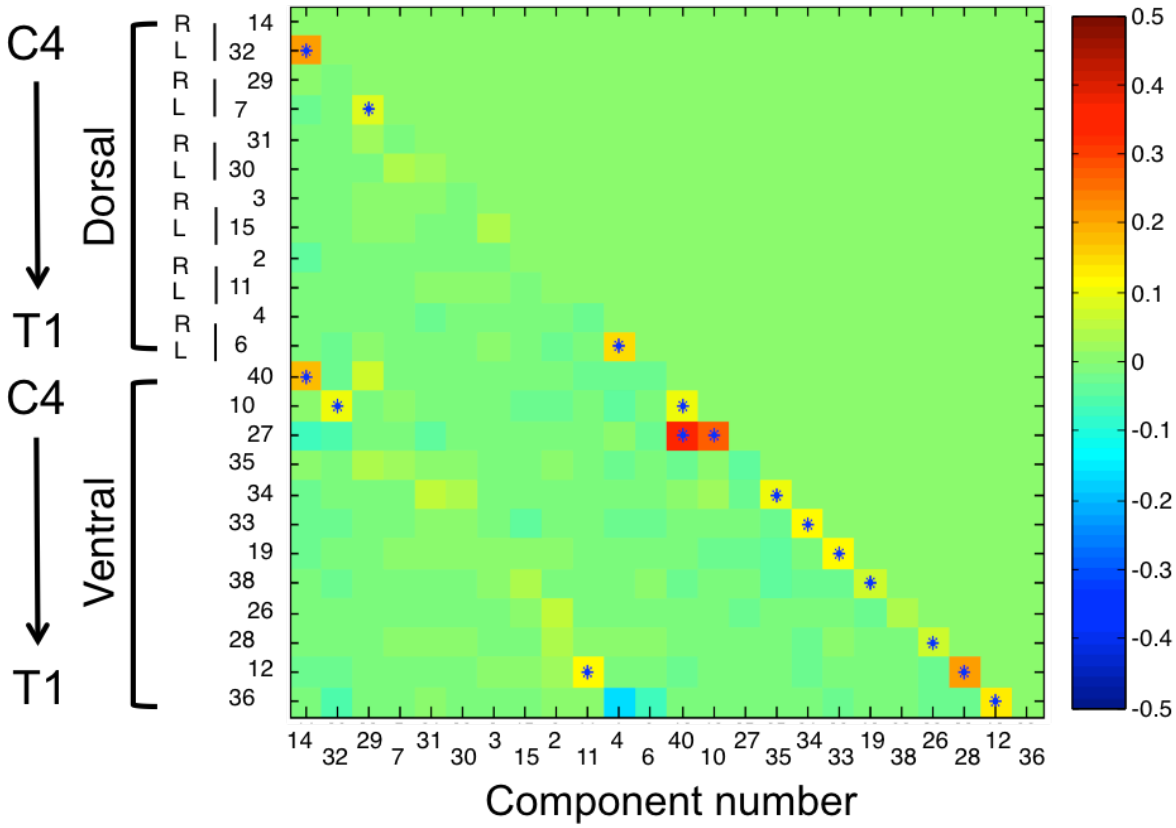

Figure S9. RSN correlation matrix using ICOV. This correlation matrix shows the similarity between two time series after regressing out the influences from all other time series and should emphasize direct connections. All other details are as in Figure 4 of the main manuscript.

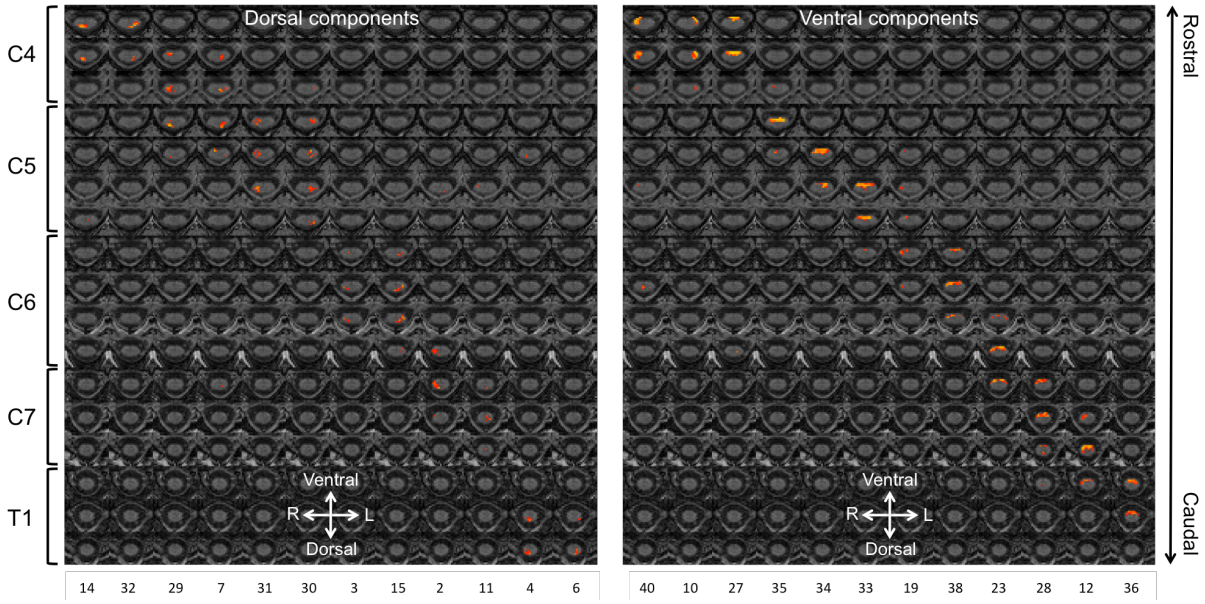

Figure S10. Split-half reliability of dorsal and ventral spinal RSNs. These maps show voxel-wise intra-class correlation coefficients (ICCs) at those voxels that survived FDR thresholding at $p < 0.05$ in our original analyses (Figure 1 & 2). Each ICC map is thresholded at ICC > 0.4 (cut-off for fair reliability) and shown in rostro-caudal direction, overlaid on transversal sections of the template T1-weighted image.

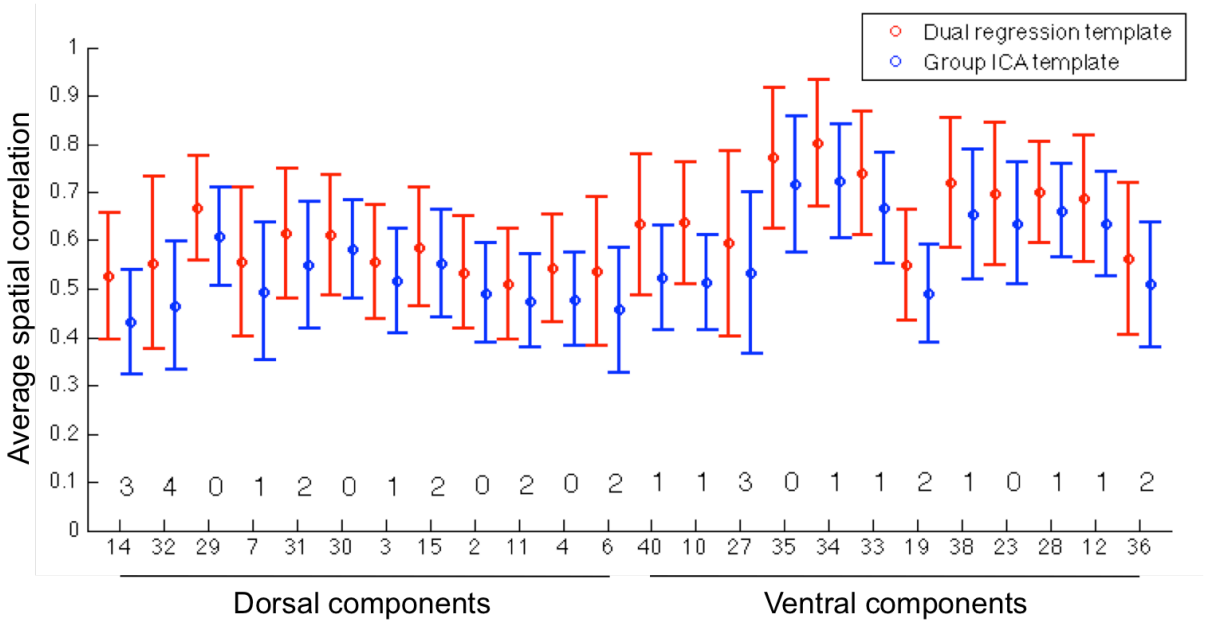

Figure S11. Reproducibility of dorsal and ventral RSNs at the individual level. We used two different template-matching procedures of single session ICAs: once against the group ICA template (blue) and once against the individual dual regression template (red). The numbers inside the figure refer to the number of times (out of 20) the two template-matching procedures disagree with regard to the chosen component; these numbers are not of primary importance here, but are provided for means of comparison with data from the brain (5).

Original IC#	40	10	27	35	34	33	19	38	23	28	12	36
Spatial corr.	0.56	0.43	0.52	0.74	0.81	0.67	0.28	0.62	0.61	0.77	0.73	0.60
Control IC#	36	25	37	40	38	39	23	30	22	15	26	12

Table S1. Spatial correlations between ventral components from the original analysis and those from the analysis on unsmoothed data. Spatial correlation was calculated using Pearson's correlation coefficient.

Dorsal components						
Original IC#	31	30	3	15	2	11
Spatial corr.	0.67	0.66	0.66	0.62	0.47	0.48
Control IC#	28	34	7	26	22	6
Ventral components						
Original IC#	34	33	19	38	23	28
Spatial corr.	0.33	0.63	0.50	0.80	0.72	0.79
Control IC#	31	10	40	2	5	3

Table S2. Spatial correlations between components from the original analysis and those from the analysis on the reduced data-set (vertebral levels C5-C7). Spatial correlation was calculated using Pearson's correlation coefficient.

Dorsal components												
Original IC#	14	32	29	7	31	30	3	15	2	11	4	6
Spatial corr.	0.23	0.14	0.76	0.74	0.65	0.82	0.79	0.74	0.64	0.51	0.27	0.26
Control IC#	38	38	18	28	14	26	24	25	11	6	36	35
Ventral components												
Original IC#	40	10	27	35	34	33	19	38	23	28	12	36
Spatial corr.	0.30	0.28	0.66	0.7	0.83	0.82	0.74	0.87	0.76	0.86	0.69	0.84
Control IC#	18	28	21	17	10	23	3	13	31	2	7	9

Table S3. Spatial correlations between components from the original analysis and those from the analysis with white-matter regression. Spatial correlation was calculated using Pearson's correlation coefficient.

Dorsal components												
Original IC#	14	32	29	7	31	30	3	15	2	11	4	6
Spatial corr.	0.52	0.40	0.68	0.64	0.49	0.73	0.79	0.49	0.46	0.32	0.34	0.43
Control IC#	58	4	30	21	26	81	15	31	5	9	39	13
Ventral components												
Original IC#	40	10	27	35	34	33	19	38	23	28	12	36
Spatial corr.	0.59	0.46	0.78	0.73	0.67	0.61	0.41	0.50	0.73	0.61	0.71	0.50
Control IC#	45	27	60	18	80	64	69	47	51	43	34	6

Table S4. Spatial correlations between components from the original analysis and those from the analysis within an extended region including the CSF. Spatial correlation was calculated using Pearson's correlation coefficient.

Dorsal components												
Original IC#	14	32	29	7	31	30	3	15	2	11	4	6
% ICC > 0.4	41.9	44.5	53.3	34.4	40.9	41.6	11.9	37.2	32.0	15.0	61.6	47.6
% ICC > 0.6	21.5	27.7	19.6	10.6	10.0	5.5	1.3	9.2	6.2	0.3	14.6	14.3
Ventral components												
Original IC#	40	10	27	35	34	33	19	38	23	28	12	36
% ICC > 0.4	76.3	80.6	85.9	79.5	81.6	63.5	27.6	63.6	60.9	62.3	64.9	57.1
% ICC > 0.6	50.0	51.0	68.4	60.1	57.4	37.5	6.7	33.7	29.1	26.0	35.8	24.9

Table S5. Split-half reliability measures for dorsal and ventral components. Intra-class correlation coefficients were calculated for each voxel that survived FDR thresholding at $p < 0.05$ in our original analysis. Here we list the percentage of those voxels that survive thresholding the ICC map using cut-offs that denote fair reliability (ICC > 0.4) and good reliability (ICC > 0.6).